Thermal Rectification to Increase Power and Efficiency of Solar-Thermal Electricity Generation

By

Mitchell Westwood

SB (Massachusetts Institute of Technology) 2011

A report submitted in partial satisfaction of the
Requirements for the degree of
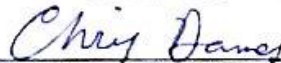
Masters of Science, Plan II

in

Mechanical Engineering

at the

University of California at Berkeley

Committee in Charge:

Chris Dames
Professor Chris Dames, Chairman

Van P Carey
Professor Van P. Carey

Semester Fall 2015

Contents

1 – Abstract

Thermal power generation of every type utilizes heat engines to produce electricity from temperature differentials. Increasing the magnitude of these differentials results in greater power output and efficiency, but in settings with oscillating temperatures, such as the hot midday sun and cold midnight sky, maximum and minimum environmental temperatures are offset in time and aren't utilized together. This work shows how, in a matter akin to rectifying oscillating AC voltage input to a near-constant DC voltage output, a periodic temperature source is rectified using a thermal diode bridge. Thermal diodes and thermal storage masses are employed to rectify this thermal signal, resulting in a larger, periodically steady temperature differential than any seen in the system's environment at any given instant. Tests are performed under a range of operating conditions and system configurations, proving a P $\propto$ (ΔT)^2 relationship that results in up to 4X power generation between rectified and non-rectified systems.

Xiaodong Zhao, a collaborator and fellow UC Berkeley MS student, performed a detailed analysis of this rectification system, producing an analytical model whose results guided much of the detailed design work presented here [1].

2 – Introduction

2.1 – Motivation

From large-scale power plants to small-scale energy scavenging, thermal power generation utilizes heat engines to produce electricity from temperature differentials. The best possible efficiency is the Carnot limit, η_C:

$$\eta_C = \frac{T_H - T_C}{T_H},\qquad(1)$$

where T_C is the temperature of the low-temperature heat sink and T_H that of the high-temperature heat source, both in kelvins. Traditional approaches to boost efficiency and output of power generation focus on raising T_H. Reducing T_C is just as helpful but is much less often pursued.

In solar-thermal power generation applications the temperature of environmental radiation oscillates widely, from the hot midday sun to the cold midnight sky However, since these periods are offset by 12 hours, at any instant a solar thermal generator never experiences the maximum possible temperature differential it will see in a full 24 hour cycle. In this sense, conventional solar thermal generators operate only at partial capacity (daytime only), using solar energy for T_H and air or terrestrial water for T_C. This is a key shortcoming of present technology: by using daytime T_{air} as their heat sink, conventional designs fail to exploit the much colder T_{sky} available at night.

2.2 – Background

While conventional power generation strategies look to improve power density and efficiency by increasing hot source temperatures, a massive cold-temperature heat sink remains virtually untouched. The far reaches of space, at temperatures below 3 K, could serve as a heat sink in a myriad of useful ways, and this resource has recently gained noteworthy attention [2-6]. Radiative cooling to the cold night sky could provide a high-quality and limitless cold-temperature reservoir for power generation applications. In solar thermal power generation applications, the

temporal offset of the highest daytime and lowest nighttime temperatures and relatively low cooling power density, q'' inhibits the utilization of this untapped resource.

Thermal rectification systems can take advantage of both these temperature extremes through the use of thermal energy storage and thermal diodes. Various designs of thermal diode concepts have been investigated [7-11]. However, these diodes concepts and others are still an active area of research, and future developments will further enable thermal rectification technology.

2.3 – Full-cycle Thermal Rectification

This work aims to rectify a periodic temperature source using a thermal diode bridge. Like common electrical rectifier circuits that use diodes and capacitors to convert an oscillating AC voltage input to a near-constant DC voltage output, this scheme with thermal diodes and thermal storage takes an oscillating temperature input, $T(t)$ and produce a quasi-steady output temperature differential, $\Delta T(t)$, or $T_H(t)$ - $T_C(t)$. This quasi-steady temperature output allows for continuous power generation through the entire temperature cycle.

Additionally, the magnitude of the resultant output temperature differential is greater than that seen by a comparable non-rectified system at any given time. This increase in ΔT could have a significant effect on output power generation. As shown above in Equation 1, the efficiency of power generation increases linearly with ΔT. At the same time, for a heat engine of thermal resistance R_E, the heat flow across the engine, q_E, also increases linearly with ΔT. Therefore,

$$P = \eta q_E \propto \frac{\Delta T}{T_H} \frac{\Delta T}{R_E} \propto (\Delta T)^2, \tag{2}$$

or output power is proportional to the square of the output temperature differential, assuming constant T_H.

Like an electrical rectification bridge, diodes and storage enable this technology, as shown below in Figures 1(b) and 1(c). During the day, solar heat is collected and flows into a high-temperature thermal reservoir, raising T_H. During the night, thermal energy flows from a low-temperature reservoir into the cold night sky, lowering T_C. Thermal diodes limit flow to these directions, minimizing energy losses. With the utilization of cold night temperatures and appropriately-sized thermal masses, this rectification system provides a temperature difference ΔT larger than any seen in ambient conditions, and it provides this gradient over the entire day-night cycle. Efficiency and power density both increase as a result.
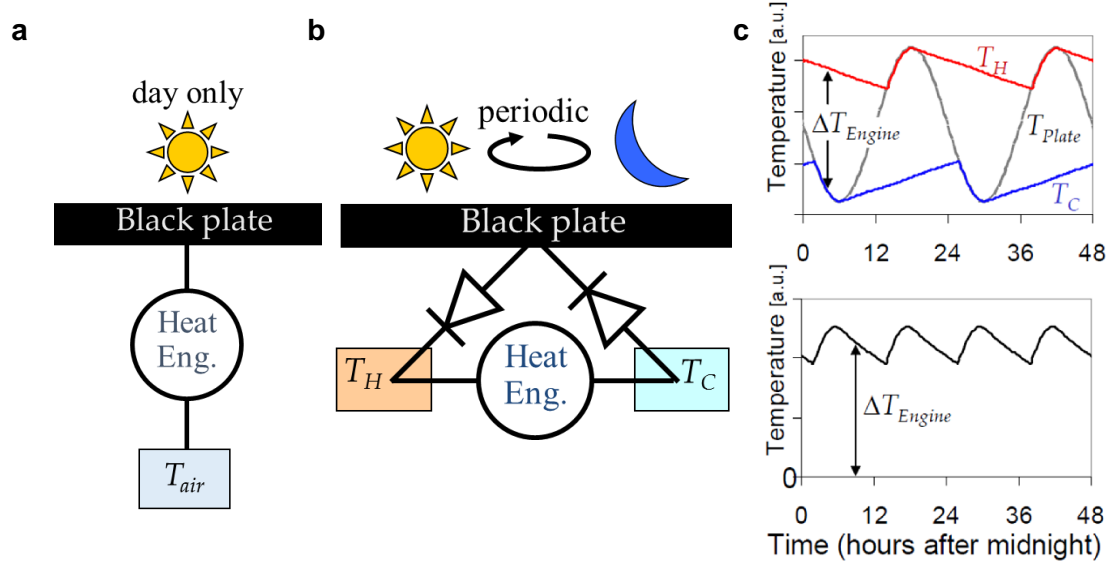
Figure 1. (a) Conventional daytime solar thermal power generation. (b) Proposed continuous generation with thermal rectification. (c, top) Modeled rectification of a periodic thermal load takes advantage of both hot and cold temperatures to increase the temperature difference seen by the heat engine [12]. (c, bottom) This rectified temperature difference is larger than that seen in a non-rectified arrangement and produces power continuously.

3 – Experimental Setup and Techniques

3.1 – Thermal Diodes

Thermal diodes are an essential element of the thermal rectification assembly. However, unlike electrical diodes, a mature technology, thermal diode concepts are an active area of research and development with still-evolving results. Therefore, an assortment of diode concepts were investigated. Thermosiphons are a well-known example of such a diode that use buoyancy to bias heat flow against the pull of gravity. However, the form factor, relative design inflexibility, operating temperature limitations, and potential for operation complications made thermosiphons unattractive for this work. More exotic concepts, such as active wetting/dewetting contacts, nanoscale geometry, temperature-specific thermal conductivity, and phase change were considered, but small reverse:forward thermal resistance ratios and more potential for complications in operation also moved design attention away from these areas. Finally, more simple mechanisms for thermal switching were considered. Unlike "passive" diodes that require no actuation for a flux direction-based thermal resistance change, several considered concepts could be better described as "active" diodes, or thermal switches, that employ a mechanical movement to change their effective thermal resistance. Like an electrical relay, a desired condition (change in heat flux direction) causes the diode device to change behavior in some way, promoting or inhibiting heat flux. Considered concepts include actuated motion of thermal contacts; triggered liquid flow; or initiated thermal expansion, as seen in wax motors.

An actuated conductive contact concept was adopted for this system for its extreme simplicity, reliability, and ease of manufacture. In forward mode, a smooth, flat surface of the thermal storage mass and smooth, flat surface of the temperature source are brought into thermal contact. Heat transfer is facilitated by a 3M 5519S 1.5 mm silicone interface pad. An interface pad was chosen over other contact aids, namely thermal grease, due to the repeated loading-

unloading condition of the diode. This pad has a rated thermal conductivity of 4.9 W/m-K and one tacky surface for permanent attachment to and enhanced thermal contact with the thermal mass.

To test the effect of pressure and contact resistance on the overall thermal resistance of the diode, a cut bar test was conducted. Brass meter bars of length 33.5 mm and face side lengths of 50.8 and 16.0 mm were constructed to match the face heating area of available Multicomp MC14734 power resistors. Three thermocouple ports were drilled through the entire width of the bars at 6.35, 12.70, and 19.05 mm from the sample face of each meter bar and packed with thermal grease. Thermocouples were inserted halfway through this length and taped in place. Temperatures were measured at each location using Omega 5TC-TT-T-40-36 T-type 0.003" thermocouples and a Stanford Research Systems SRS630 thermocouple monitor. Heating was applied with a single power resistor and an Agilent N5750A DC power supply; heat was removed using an available cold plate with internal cooling water channel. After constructing and inserting between meter bars a sample of the 3M interface pad with similar 50.8 and 16.0 mm side lengths, insulation was wrapped around the entire meter bar and sample assembly. An overhead weight stage was created to allow for even and controlled pressure application from above. A separate 50.8 by 16.0 mm section of insulation was cut above the top-mounted heater, allowing pressure to be applied only to the meter bar and sample stack and not to the surrounding side insulation. While 3M literature declared the interface pad thermal conductivity to be tested at a pressure of 68.9 kPa (10.0 psi), tests were performed across a 6.9 to 68.9 kPa range (1.0 – 10.0 psi). While smaller weights were used for pressure application to the 50.8 by 16.0 mm cut bar test section, a 50 lb calibration weight borrowed from UC Berkeley's Hesse Hall was utilized for pressure application at the final diode size.

At a desired operating pressure of 10.6 kPa (1.54 psi, or 50 lbf applied to the diode area of 32.4 in^2), the forward resistance of the diode interface was found to be 1.07×10^{-3}/A K/W, where A is the diode contact area in m^2. In the final as-built system, the diode contact area was 2.09×10^{-2} m^2 (5.4 x 6.0 in), resulting in a diode forward thermal resistance (R_F) of 5.13×10^{-2} K/W. While resistance measurements from the cut bar test are repeatable to ±5%, future work would benefit from an effort to validate this proposed area scaling relationship by testing a full-size diode pad resistance at operating pressure.

In the reverse mode, thermal storage mass and temperature source surfaces are brought out of contact, and a layer of insulation is placed in between. As detailed more fully later, Aspen Aerogels Spaceloft insulation was used. This insulation has a rated thermal conductivity of 0.014 W/m-K, and a 30 mm-thick layer was assembled. Using the same diode contact area, this thermal resistance in the reverse, or backwards mode (R_B) is found to be 1.03×10^2 K/W. The resulting diode reverse:forward thermal resistance ratio is 2008:1. While this "active" diode concept requires mechanical actuation, this large resistance ratio and its exceedingly simple design make it a perfect candidate for this work. These resistances are summarized with other relevant system thermal resistances described in following sections in Figure 2 below.
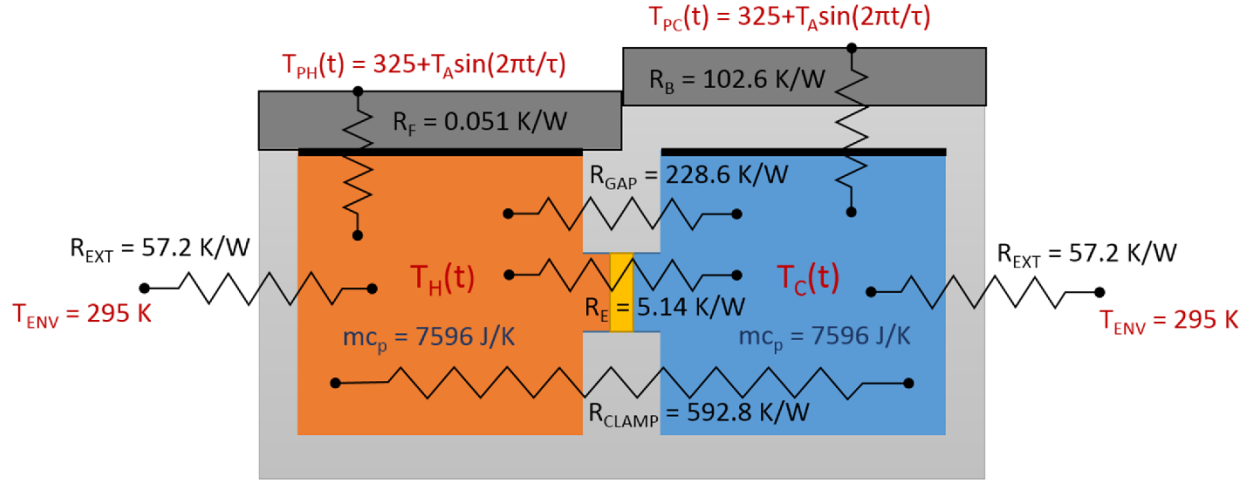
Figure 2. Thermal resistances of the thermoelectric heat engine (R_E), diodes in forward mode (R_F), diodes in reverse or backwards mode (R_B), across the gap between masses (R_{GAP}), between masses due to the thermoelectric clamping rods (R_{CLAMP}), and from each mass to the external environment (R_{EXT}). These resistances are subject to temperatures of the environment (T_{ENV}), hot and cold temperature plates ($T_{PH}(t)$, $T_{PC}(t)$), and the hot and cold thermal storage masses ($T_H(t)$, $T_C(t)$). Also displayed are thermal storage capacities of the thermal masses (mc_p).

3.2 – Heat Engine

To generate useful power from our rectified thermal source, several heat engine types were considered. While Stirling, Rankine, and other engine cycles can be relatively efficient, their moving parts and risk of failure, as well as the complications of energy measurement or conversion, suggested they might not be the right fit for this initial study. Instead, a thermoelectric module (or thermoelectric generator, TEG) was chosen for its solid state robustness; simple, electrical power output; compact form factor; reliability; and ease of overall integration. While the efficiency of thermoelectric devices can be less than other heat engines, identical thermoelectric modules were used between comparative tests, allowing for sufficient demonstration of the proposed rectification method and its relative effects.

Laird ThermaTEC Series HT9,3,F2,2525 25 x 25 mm thermoelectric modules were selected for the rectification assembly. These modules can accommodate power generation applications at temperatures up to 175 °C, making them a perfect fit for the system's needs. As determined by Laird's AZTEC software (online), the thermal resistance across the heat engine (R_E) is 5.14 K/W. This results in a R_E:R_F ratio of 100.2:1, and a R_B:R_E ratio of 20.0:1. Early simulations [1] suggested improvements in the R_E:R_F ratio more positively impacted overall performance than improvements in the R_B:R_E ratio, prompting diode contact areas to be sized as they were.

To produce the maximum available power from the thermoelectric module, care was taken to match its internal electrical impedance with an accompanying external circuit. A matching value of 0.40 Ω was given in the Laird technical information for this module, but a decade box was used to provide a second check on this number. Voltage and current were measured using two multimeters while circuit resistance, R_C was changed in 0.01 Ω increments with the decade box, and resultant power was monitored. Indeed, an external resistance of 0.40 Ω was found to produce the greatest electrical power from the thermoelectric module at two different temperature differentials, and this circuit resistance was maintained throughout testing.

6

3.3 – Thermal Mass

6061-T6 aluminum blocks were used for thermal storage. Several other storage mass materials were also considered, including various metals, concrete, and water. Though water and concrete have thermal storage and cost benefits, aluminum was chosen as the storage material thanks to its adequate thermal storage density (quantified by ρc_p), high thermal conductivity, ease of use and manufacture, and reasonable cost.

Two cubes of nominal 152.4 mm (6 in) side length were used to create the storage masses. Positioning the 5 mm-thick thermoelectric module between two large, flat faces of the masses would result in a corresponding 5 mm-thick gap across which heat could leak between masses. Therefore, material was removed from one face of each of the mass to produce a boss upon which the thermoelectric module could be mounted. These bosses served as a thermal bridge between the masses with the thermoelectric generator sandwiched in the middle, as shown below in Figure 3. As a result, the remainder of the gap between the masses was increased to 30 mm, allowing for six times the insulation and a reduction of thermal leakage by an equal amount. The resulting thermal resistance of this gap leakage path (R_{GAP}) was calculated to be 229 K/W, 44.5 times larger than that of the heat transfer path through the thermoelectric module. It is worth noting that this material removal process reduced the final diode contact area to 2.09×10^{-2} m^2 (5.4 x 6.0 in) from the original nominally 6 inch side length dimensions.
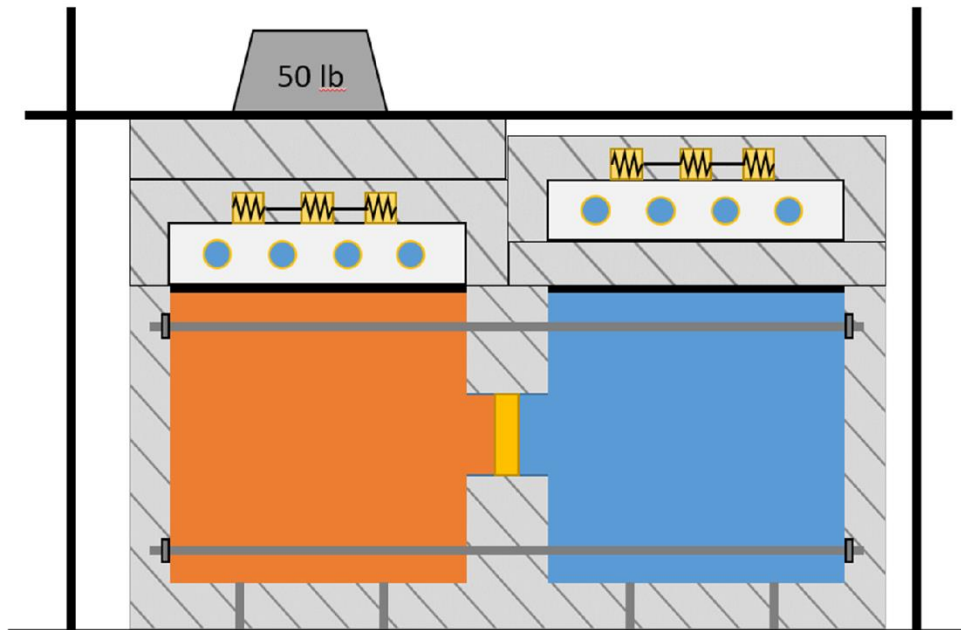

Figure 3. Schematic of mechanical test assembly. Thermal storage masses with thermoelectric module mounting features are clamped together with 8-32 threaded rods, Belleville washers, and nuts to provide stable contact pressure on faces of the thermoelectric heat engine. Polycarbonate cylinder standoffs below thermal storage masses reduce compressive deformation of insulation under the masses. A weight stage promotes even loading of the temperature plate assembly on the conductive interface pad when diodes are in forward mode (left). Insulation separates the plate from the mass in the diode's reverse mode (right).

A fly cutter and Bridgeport milling machine were used to produce flat contact faces on the masses for the thermal diode pads and the thermoelectric module. A slow final pass produced a shiny surface, indicating a smooth surface profile. After these facing and milling material removal

steps, the final volume of the masses was determined (3.14×10^{-3} m^3 each), and using an aluminum density of 2700 kg/m^3 and specific heat of 896 J/kg-K, an effective heat storage capacity of 7596 J/K per mass was determined and used in final design calculations. A lumped capacitance model was proposed and confirmed for these masses. A calculation using Spaceloft insulation on five of the thermal mass faces and the forward diode pad on the sixth face produces an effective surface heat transfer coefficient of 155 W/m^{2}K, resulting in a Biot number of 0.140. This value allows a uniform temperature to be assumed across the entire mass. This was confirmed in testing with several temperature measurement points on each mass which always agreed to within ±0.5 K.

3.4 – Insulation

To minimize parasitic thermal leakage to the environment, layers of insulation were added to the external faces of the mass and thermoelectric module assembly. As previously mentioned, insulation was also added in the gap between storage masses to inhibit this leakage path. While insulation thickness was of little concern on external faces, increasing the gap between thermal masses to accommodate thick insulation could result in temperature differentials along the length of the aforementioned thermoelectric mounting bosses. Therefore, an effort was made to find insulation with impressive characteristics at reasonable thicknesses. Aspen Aerogels Spaceloft insulation was selected for its relatively low thermal conductivity of 0.014 W/m-K. This insulation was sourced in 10 mm-thick sheets, and three sheets were stacked to create a 30 mm insulation layer on all external faces and the internal gap between masses. As previously stated, the resulting thermal resistance between storage masses (R_{GAP}) is then 228.6 K/W. The thermal resistance between each mass and the external environment (R_{EXT}), through four mass faces (not counting the "top" diode face and the face between thermal masses) is 57.2 K/W, or slightly less than one fourth the R_{GAP} value. See Figure 2 for these and other system thermal resistances.

Proper thermoelectric module installation calls for a face mounting pressure of 689 kPa (100 psi), and this was achieved by clamping the storage masses together using four 8-32 316 stainless steel threaded rods, Belleville washers, and nuts. Oversized through-holes were drilled across the entire lengths of both thermal masses using specialty extra-long 3/16" drill bits, and these washers and nuts clamped the masses together from each face furthest from the other mass. This made for as long a thermal contact path as possible. Ideally, these threaded rods (with cross sectional area 7.92×10^{-6} m^2) would only be in thermal contact with each mass at their very ends, across the length of both masses (a total length of roughly 300 mm). Four of these rods in parallel produced an expected clamp thermal resistance (R_{CLAMP}) of 592.8 K/W. Belleville washers aimed further to increase contact resistances at the end interface between rod and thermal mass and to stabilize the contact loading pressure. Nut and washer assemblies were torqued according to typical bolt torque-tension load relations to 0.09 Nm to reach the desired rod tension of 111 N (25 lbf) and thermoelectric clamping pressure of 689 kPa (100 psi). While contact of the rod inside the mass through-hole and radiative or convective coupling between the rod and mass was likely, these effects were thought to be relatively small. Finally, in addition, thermal standoffs were incorporated below the thermal masses to reduce compression of insulation under loading. These standoffs were made from polycarbonate cylinders and had thermal resistances of 1028 K/W. Again, major system thermal resistances are summarized in Figure 2.

3.5 – Boundary Condition and Operation

A sinusoidal temperature profile was chosen as the rectification system's boundary condition. This profile well illustrates the effect of thermal rectification, satisfactorily meets realistic solar conditions [1, 13], requires relatively simple laboratory hardware and instrumentation, and is easy to use through initial prototyping. A second boundary condition that was considered [1] utilizes a combination of heat flux and thermal resistance to model as close to a realistic day and

night sky condition as possible. This model assumes daytime solar exposure is most realistically modeled using a time-dependent solar heat flux, while day and night cooling is more accurately modeled using convection and radiation to effective local and atmospheric temperatures, respectively. However, while this latter boundary condition aims to replicate a natural environment more closely, the sinusoidal temperature profile was instead chosen for this first experimental demonstration for its simplicity and illustrative merit.

Since the sinusoidal temperature source needs to both heat the hot mass and cool the cold mass, it must have both heating and cooling capability. To accomplish this, a combination heating and cooling assembly was designed. The cooling base of this assembly is a Wakefield-Vette 180-20-6C aluminum cold plate. Like the aluminum thermal storage masses, for enhanced thermal contact, one surface of each cold plate was cut flat and smooth using a fly cutter and Bridgeport milling machine. This plate has a rated 0.038 K/W thermal resistance between the water temperature and plate surface temperature at the recommended 1.0 gpm flow rate. A laboratory city water flow through this cold plate supplied the assembly's cooling power. As later described, water flow and resulting cooling power were variable with time. For heating, a set of Mulitcomp MC14734 power resistors were mounted to the top of the cold plates using thermal grease. Each 100 Ω resistor is rated for 50 W of heating, resulting in a maximum current of 0.71 A or maximum voltage of 70.7 V. These resistors were powered using an Agilent N5750A DC voltage source with a 5 A, 150 V limit. Therefore, six resistors were wired in parallel, allowing for 4.2 A of current at 70.7 V, providing a maximum of 300 W of heating. Simulation models [1] suggested peak heating needs on the order of 100 W, so this heating capability was deemed adequate. AWG 14 wire was sourced for this assembly for its relatively high current demand. These temperature plates are seen with other instrumentation components in Figure 4 below.
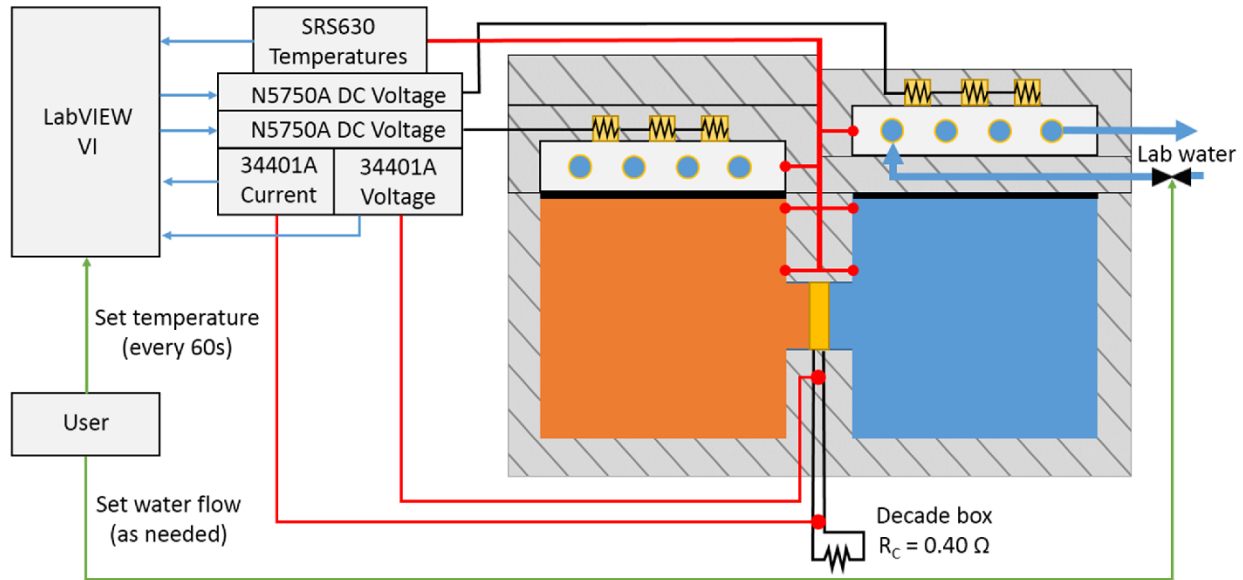

Figure 4. Schematic of instrumentation and controls in the thermal rectification testing assembly. Two temperature plates set to identical temperatures via user input are seen in forward diode (left) and reverse diode (right) mode. LabVIEW is used to control these plate temperatures through input temperature signals via a Stanford Research Systems SRS 630 thermocouple monitor, internal PID control, and output DC voltage supplied to resistor assemblies on the plates. Users can also modify water flow rates to assist this process. Agilent 34401A digital multimeters are used to measure thermoelectric voltage and circuit current via a sense resistor to calculate electrical power.

To provide an accurate temperature boundary condition, a LabVIEW Virtual Instrument (filename "Lab heat source and sink.vi") with PID control was constructed. A built-in PID function allowed for steady state temperature control using an input temperature (read from a thermocouple described in the following section), desired temperature (set by the user), PID gains (set by the user), and a resulting output voltage command sent to the DC voltage supply. It was hoped that a constant cooling water flow and PID-controlled heating could supply all the heating and cooling needs of an entire temperature profile. However, in operation, it was observed that the water flow needed to be controlled as well. At the highest temperatures of the temperature profile, when resistive heating is used to maintain an elevated temperature while the plate also "charges" the hot mass, anything above the smallest water flow was found to decrease the temperature below its set point, even at maximum heating power. At the same time, this small water flow did not have the cooling power to drive the plate to its lowest temperatures while "discharging" the cold mass at the bottom of the temperature profile. Therefore, an amount of user effort was required to control water flow. While PID control maintained temperatures to a reasonable degree, water flow needed to be reduced for plate heating and increased for plate cooling. Great care was needed, however, to modify water flow rates as gradually as possible. This was performed with an in-line needle valve. Especially at elevated temperatures, small changes in water flow were often found to drive the plate temperature too far from its set point, ruining a test. Greater heating capacity (allowing for full PID control with high background water flow) or more accurately controlled water flow would be an excellent upgrade to the laboratory system in the future. Built-in temperature command profiles would also serve as a beneficial upgrade to the system. Instead of an automated sine curve input, test operators forced a piecewise approximation temperature curve by changing the set point every 60 seconds to pre-calculated values. This took time and attention, and it served as a point of error in several discarded tests. This 60-second discretization of the sine profile is hardly evident in temperature plots, but many headaches could be saved by integrating a smarter curve generation input program into LabVIEW.

Due to geometric constraints, two temperature plates were used in each test for the two thermal diodes. Optimally, both thermal diodes should be exposed to the same plate temperature. However, the as-built diode design resulted in a change in the diode thickness of 30 mm upon forward and reverse switching. No simple and cost-effective ways to apply one flat plate to two diode surfaces of changing height were developed. Therefore, two temperature plates, driven to the same temperature $T_P(t)$, were used to model one single plate. Two independent sets of cold plate, resistor assembly, power supply, and water loop assemblies were produced, as shown in Figure 4. Each operated independently and according to its own needs. This independence of the two systems was critical in practice, as the environmental loads of these plates differed when one diode is in forward "charging" mode and the other is not. As seen later in testing results, these independently controlled plates maintained their desired sinusoidal temperature profiles well and are visually indistinguishable from each other in system temperature plots.

3.6 – Instrumentation
LabVIEW was used as a simple and effective way to collect system data and drive the forcing temperature profile. As previously described, two independent Agilent N5750A DC power supplies were used to provide power to PID-controlled resistor banks through built-in LabVIEW functionality. To observe system temperatures, a Stanford Research Systems SRS630 thermocouple reader was utilized and also controlled through LabVIEW. The thermocouple reader monitored temperatures through a series of Omega 0.003" Teflon-coated T-type thermocouples. Finally, power measurements were taken using two Agilent 34401A multimeters. One multimeter recorded output voltage across the thermoelectric module leads. A second multimeter recorded

the voltage drop across the very well-known decade box resistance, or sense resistance of 0.40 Ω, allowing the circuit current to be calculated. This method of current resistance after an attempt to measure in-line current directly failed, thanks to the significant burden voltage produced by the 34401A multimeter. These voltage and current values were multiplied to produce the output power of the thermoelectric module. These components can be seen in the instrumentation schematic in Figure 4 and an image of the thermal rectification testing assembly shown below in Figure 5.
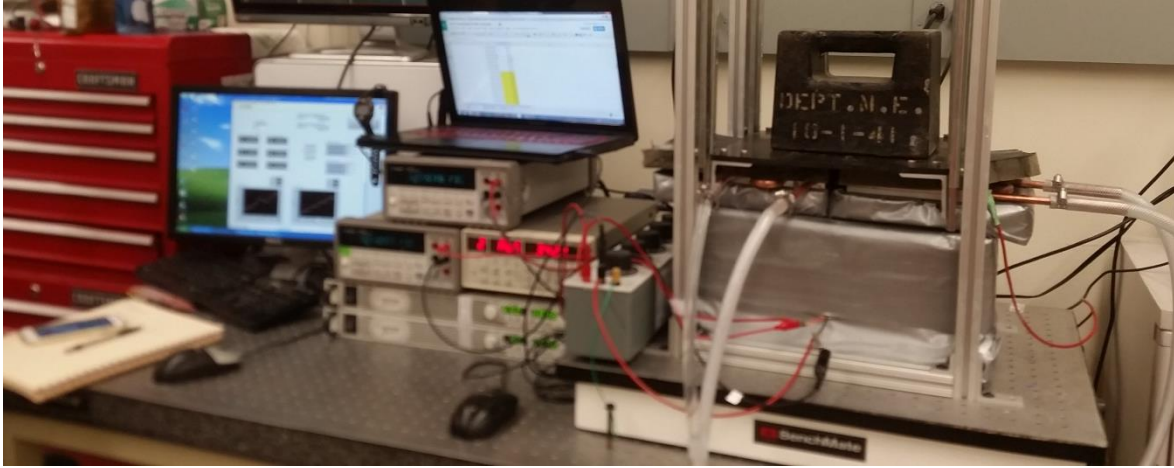

Figure 5. Thermal rectification testing assembly. LabVIEW operation is facilitated by user input of an array of calculated sinusoidal temperature points. Two power supplies, two multimeters, a thermocouple monitor, and decade box are seen. A fully-insulated thermal mass assembly sits below two diode insulation pads, temperature plates, and weight stage with 50 lb weight for pressure application (right). Operators lifted this weight, inserted or removed insulation, and replaced the overhead weight to change the thermal resistance of each "active" diode.

4 – Results

4.1 – Rationale and Test Plan

Five rectification tests were performed and are summarized below in Table 1. The first three of these tests examined the fully-rectified system with optimized diodes and masses, as shown in Figure 6(a). This system was exposed to a source temperature profile, $T_P(t)$ of the form

$$T_P(t) = 325 + T_A\sin\left(\frac{2\pi t}{\tau}\right), \tag{3}$$

where T_A is the sinusoidal amplitude and τ is the sinusoidal period. Laboratory heat engine throughput, thermal mass size, and diode resistances were designed with 25 K amplitude and one hour period in mind. A test with these conditions was performed first and is referred to as the "baseline" experiment. The effect of changes in thermal source frequency was then investigated by reducing the frequency of the temperature profile by 50%. This two hour period test is referred to as the "frequency dependence" test. Similarly, an "amplitude dependence" test investigates the effect of changes in the temperature signal amplitude by reducing the profile amplitude by 50% to 12.5 K.

Two additional tests served to investigate the effect of rectification as compared to a non-rectified system. While the rectified system employs thermal storage to smooth temperature profiles, uses diodes to bias heat flux, and utilizes cold temperatures to increase overall ΔT, many large-scale solar thermal power generation systems also utilize the first two of these three

11

functions. Molten salts or other fluids are often used for overnight thermal storage, and this working fluid does not flow through solar collectors at night – a form of "active" diode, in a way. However, these systems still don't utilize the low-temperature heat sink of a cold night T_{sky}. Therefore, a "solar thermal" comparison test is performed where a diode and thermal storage are used on the "hot" side of the system, but a constant average ambient temperature, T_{amb} is used as a cold sink. This assembly is shown in Figure 6(b). Finally, a completely non-rectified system is investigated. Here, a thermal engine is employed between an oscillating temperature source and a constant average, ambient temperature heat sink. Since this use case most closely resembles a "waste heat scavenging" application, the test is referred to as such. This system is shown in Figure 6(c).

Table 1. Laboratory tests performed. These tests examine the effect of test conditions and device configurations on system performance. Source average temperature, T_{AVG} is 325 K in all cases.

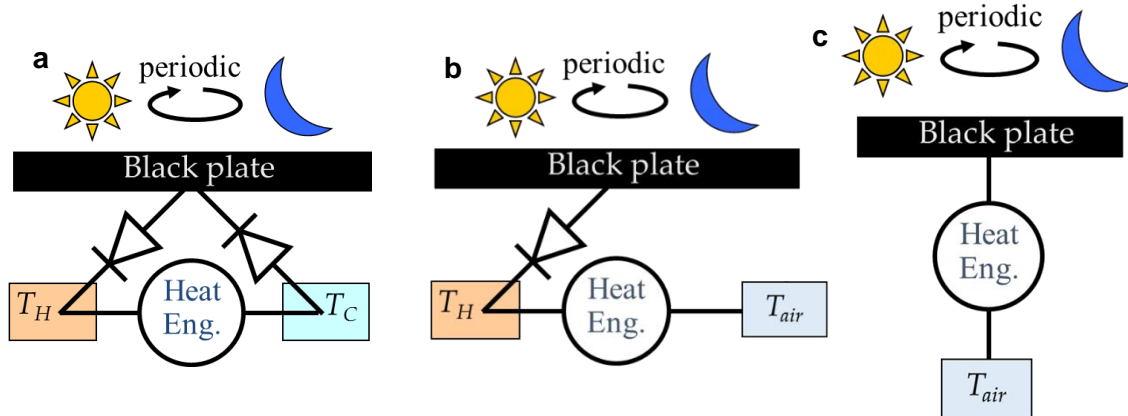| Test	"Baseline"	"Frequency Dependence"	"Amplitude Dependence"	"Solar Thermal"	"Waste Heat Scavenging"
T Amplitude, T_A (K)	25	25	12.5	25	25
T Period, τ (hours)	1	2	1	1	1
No. of Diodes, Masses	2, 2	2, 2	2, 2	1, 1	0, 0
Component Model	Figure 6(a)			Figure 6(b)	Figure 6(c)

Figure 6. (a) Baseline rectification test scheme. (b) "Solar thermal" comparison application with diode and thermal storage mass only on the "hot" side of the system. (c) "Waste heat scavenging" comparison application with no diodes or thermal storage masses. Air temperature T_{air} is set to the source temperature average temperature T_{AVG} = 325 K. See also Table 1.

4.2 – Baseline: One Hour Period, 25 Kelvin Amplitude

A "baseline" test was performed using a temperature signal with a period of one hour and amplitude, T_A of 25 K (temperature range from 300 to 350 K). To best characterize each set of conditions, tests were run a number of periods to a "periodically steady" state where behavior between periods was nearly indistinguishable to the limits of measurement precision. While this periodically steady behavior most easily allows comparison between tests, the full "warm-up" time is shown below in Figure 7. For this test, all plates and masses begin at an average "cold start"

average temperature of 325 K, shown with a dashed line. Tests reliably required between 3 and 4 full periods to reach "periodically steady" from a cold start, and only periodically steady behavior is shown in later results (Figure 9 and Figure 10). Both temperature and power output profiles are seen below in Figure 7.
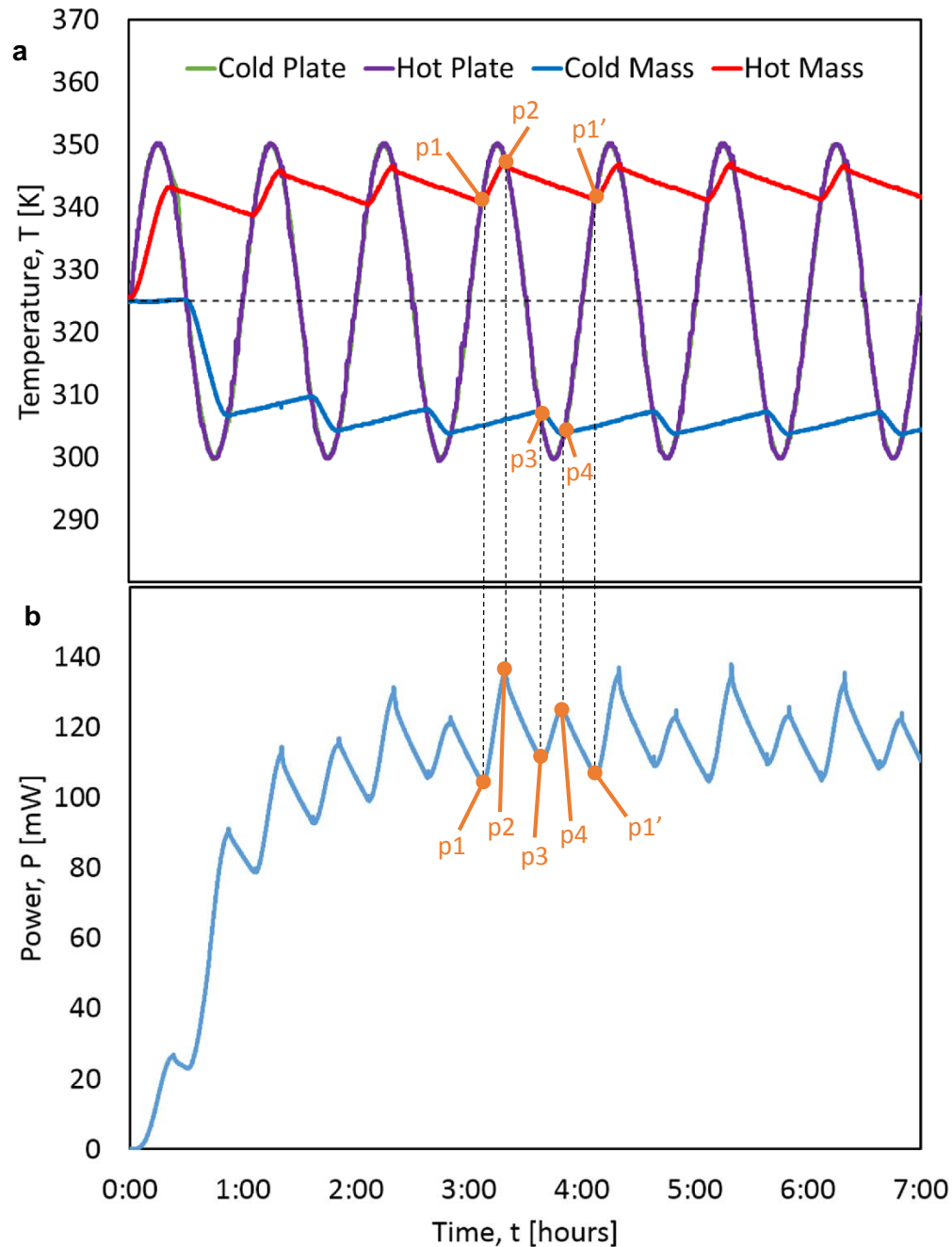

Figure 7. "Baseline" experiment. (a) Temporal temperature profile of thermal storage masses subject to rectified sinusoidal temperature signal with one-hour period and 25 kelvin amplitude. Hot and cold plate temperatures are visually indistinguishable. (b) Resultant electrical power produced by thermoelectric heat engine between thermal storage masses.

Several aspects of system behavior are expected. Hot mass temperatures increase during a "charging" period when $T_{plate} > T_{mass}$ (p1-p2), and they decay toward the cold mass temperature (through the thermoelectric module) during the remaining "discharge" period (p2-p3-p4-p1'). Symmetric behavior is seen in the cold mass temperature – cooled by cold plate temperatures (p3-p4), and warmed by heat flow through the thermoelectric (p4-p1'-p2'-p3'). This cycling of mass temperatures results in a cycling of the output power. The temperature differential across the heat engine, ΔT increases when either mass is "charged" by plate heating or cooling (p1-p2 and p3-p4). When neither mass is in this charging period, the decay of both mass temperatures toward each other reduces ΔT and the resulting power output. Finally, as described earlier, two temperature plates were used to provide near-identical temperature boundary conditions to the hot and cold side diodes. However, brief disturbances occasionally brought these temperatures slightly apart. This is seen in small instances where the green Cold Plate curve is seen deviating from the overlaid purple Hot Plate temperature, such as t = 0:20 in Figure 7. However, these instances were very rare, and the magnitude of this deviation was deemed inconsequential to overall system performance.

However, several aspects of operation were initially unanticipated. For example, a "double period" of sorts is seen in the thermoelectric power output. Even in the last few periods of periodically steady behavior, alternating high and low power peaks are evident. In a completely symmetric system, this shouldn't be the case. However, the reason for this lies in another visually-evident phenomenon. As seen in the system's temperature profile, the temperature of the hot thermal storage mass "decays" more rapidly than the cold mass temperature (p2-p1' vs p4-p3'). With symmetric insulation, this was unexpected. However, this effect is owed to the system's external ambient temperature. The applied sinusoidal temperature profile is centered about 325 K. However, ambient room temperatures during testing were closer to 295 K. As a result, the hot side thermal storage mass lost a disproportionate amount of heat to the environment. Figure 2 again illustrates these heat leakage paths. Centering the applied temperature profile about the environmental ambient temperature or artificially driving an ambient temperature to the average of the applied temperature profile should "correct" this asymmetry, if desired.

Another unanticipated behavior was observed in the power output profile. Seen at every peak and trough of the curve is a small spike in power. When investigated more thoroughly, it was found that this power spike actually occurred the entire duration the overhead 50 lb mass was removed to "flip" a diode, a period usually between 15 and 20 seconds in length. This explanation matches the profile behavior – each spike occurs when a diode is flipped to forward mode for "charging" or back to reverse mode. Follow-up tests were conducted that showed a small but reliable power increase with the removal of the 50 lb mass. This is likely due to an effect where the presence of the 50 lb mass shifts the bolted thermal mass assembly such that contact pressure on the thermoelectric module is reduced. This slightly reduced pressure causes a small increase in thermal contact resistance at the interface, reducing heat flux and output power. In future designs, a pressure application system should be designed that does not cause this effect.

Finally, more notably in additional results shown below, an unexpected behavior of the temperature PID control was observed. As previously described, when the plate temperature progressed below the hot storage mass temperature (p2), a manual operation was performed to switch the diode from forward (contact via interface pad) to reverse (inserted layer of insulation) modes. This particular operation, the hot side diode forward to reverse switch, often cooled the plate by a few kelvins, likely due to convection with the environment and the application of relatively cool insulation. However, this drop of a few kelvins often caused an overcompensation in the PID control. In several examples, one can see a ripple in the purple "hot plate" temperature not seen in the cold plate, for example at time t = 2:40 in Figure 9 (middle). This effect, however,

was deemed to have little impact on the mass temperatures, since the diode was then in its insulation reverse mode. Additionally, this effect was mitigated with operating practice and improved technique – namely, reinserting the insulation pad with its warmer side facing the hot plate.

4.3 – Frequency and Amplitude Dependence: Two Hour Period and 12.5 Kelvin Amplitude

While the "baseline" assembly test shows interesting results, further insights can be gained by varying operating conditions. As previously described, a "frequency dependence" test with doubled two-hour period was performed, as was an "amplitude dependence" test with reduced 12.5 K amplitude. The periodically steady temperature profiles, power profiles, and average power output can be seen below in Figure 9. Results of these tests are summarized in Table 2.

The effects of frequency and amplitude on system behavior are clearly seen. In the "frequency dependence" case, a visual check shows longer "discharge" periods resulting in higher magnitude decay of thermal mass temperatures. This results in a slightly reduced average ΔT between masses and across the thermoelectric module, and the corresponding reduction in power. This system only produces 89.7% the power output of the "baseline" case (105.3 vs 117.4 mW).

A stronger effect is seen with a change in thermal signal amplitude in the "amplitude dependence" case, however. Unsurprisingly, a thermal signal with amplitude reduced by 50% produces a ΔT between masses that's correspondingly reduced and a greatly reduced power output. This operating condition resulted in 27.9% the power of the "baseline" case. How does this compare to the proposed $P \propto (\Delta T)^2$ relationship? This power output would seem to correspond to a ΔT change of less than 50% between cases. As a matter of fact, however, this is actually what is observed. This is likely due to the reduced magnitude of absolute ΔT across the thermoelectric module. Since each mass is subject to a smaller decay-forcing temperature differential (that being the difference between the thermal mass temperatures), the mass temperatures decay less quickly, and a temperature differential remains that is slightly higher than 50% the "baseline" case. In addition, the largest ΔT of the system, between T_H and the ambient temperature, is also reduced in this scenario. Though the applied temperature signal amplitude decreases by 50%, the average ΔT between the thermal storage masses decreases by 47.3% (from 38.3 K in the "baseline" test to 20.2 K in the "amplitude dependence" test). A quick check maintains this $P \propto (\Delta T)^2$ relationship: 52.7% of the "baseline" ΔT, when squared, should produce 27.8% the output power (compared to the observed 27.9%). Therefore, this model still holds true, and the near-quadrupling of output power with doubled input temperature amplitude is realized. This relationship is investigated more directly in the following section and in Figure 8(a).

4.4 – Comparison Cases: "Solar Thermal" and "Waste Heat Scavenging" Assemblies

Two non-rectified comparison cases were examined. As previously described, large-scale solar thermal power generation systems can utilize both thermal storage and "active" diodes via overnight working fluid storage and the on-off switching of this working fluid flow. Therefore, a "solar thermal" comparison test is performed where a hot side diode and storage mass are utilized, but a constant average "ambient" temperature is applied as a cold side heat sink by holding the cold side thermal storage mass at a fixed T_{AVG} with temperature plate heating and cooling.

Additionally, a completely non-rectified assembly test is performed. Without diodes or storage masses, the thermoelectric module is subject to a sinusoidal temperature profile on one side and a constant average "ambient" temperature heat sink and source on the other. This "waste

heat scavenging" application is the only one where heat flux is seen in both directions across the thermoelectric module, but this power generation is a positive quantity at all times. While "baseline," "amplitude dependence," "frequency dependence," and "solar thermal" tests could be performed with identical test assemblies, the "waste heat scavenging" test required a modified system. While the LabVIEW PID plate temperature control method satisfactorily maintained a constant T_{AVG} in the cold side thermal storage mass in the "solar thermal" test as previously described, this control method was not well-suited to control the temperature of the much larger thermal storage mass to the desired sinusoidal temperature profile at the required speed and precision needed for this experiment.

Therefore, these masses were eliminated, and a new assembly consisting of an identical thermoelectric module sandwiched between the centers of the temperature plates was created. Thermal spreaders consisting of aluminum blocks (1.5 x 1.5 x 1.0 in) were placed between the plates and the thermoelectric module to eliminate any local temperature effects at the plate interface that might impact the small module area more than a large mass diode face. This modified system allowed for accurate control of both sinusoidal source temperature and constant sink temperature profiles. However, the modified system used the diode's overhead weight system to apply pressure to the faces of the thermoelectric module instead of the previously used mass-clamping technique. In addition, a second Laird ThermaTEC Series HT9,3,F2,2525 thermoelectric module was used. Finally, while temperatures on either side of the thermoelectric module were measured on the thermal mass in the original assembly, this modified assembly required that these temperatures were measured on the thermal spreaders. These three changes in the thermoelectric module's local environment mean that for a given measured temperature difference across the module, the resultant power output of the "waste heat scavenging" test thermoelectric module is different than that of module in the "baseline," "frequency dependence," "amplitude dependence," and "solar thermal" tests, between which contact pressure and other local interface characteristics are identical. This effect was investigated more clearly by comparing TEG power to the temperature difference across the TEG module in Figures 8(a) and 8(b). While these curves both show clear $P \propto (\Delta T)^2$ relationships to a high degree, they also show the effect of the changing assembly environment on thermoelectric module power output. This 19% increase in output power for the "waste heat scavenging" case must be considered before any comparisons between this case and other tests are made.
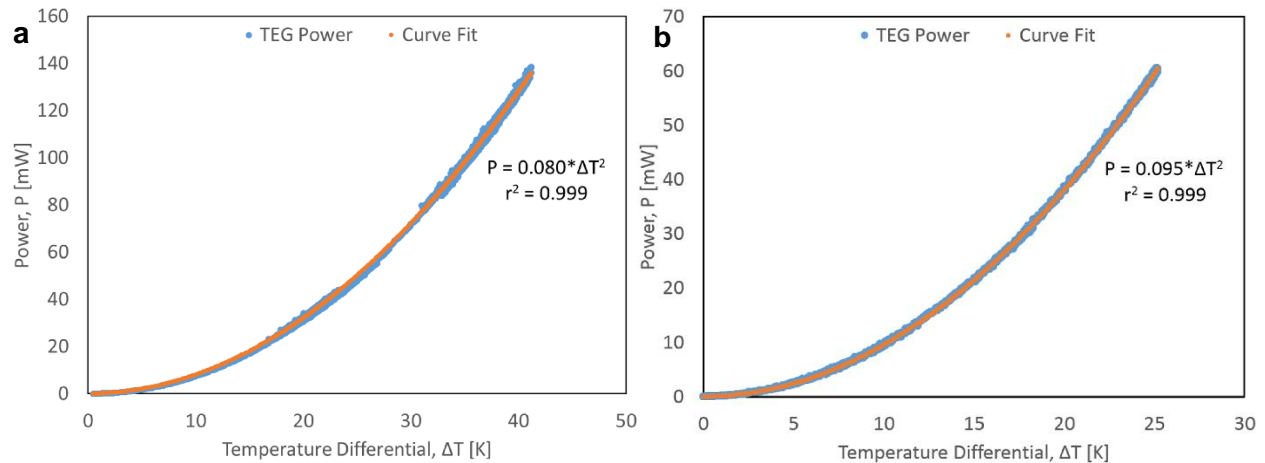

Figure 8. Thermoelectric module power output as a function of temperature differential across the module. Both curves show a close fit with a $P \propto (\Delta T)^2$ relation to an r^2 value of 0.999. (a) Power output across all "baseline," "frequency dependence," "amplitude dependence," and "solar thermal" tests. (b) Power output in "waste heat scavenging" test. This demonstrated difference in TEG power between test assemblies should be noted in comparisons between tests.

Test assembly concepts are detailed in Figure 6. Results of the tests and the comparative "baseline" test are detailed in Figure 10. These experiments and results are summarized below in Table 2.

Table 2. Summary of testing results from Figure 9 and Figure 10. Rectification is shown to increase power output drastically over non-rectified cases. This stems from maximum utilization of environmental temperature extrema to increase heat engine temperature differentials, also shown by the "amplitude dependence" case. *Power generation variation detailed in Figure 8 should be noted when reviewing "waste heat scavenging" power output values.

Test	"Baseline"	"Frequency Dependence"	"Amplitude Dependence"	"Solar Thermal"	"Waste Heat Scavenging"
Source T Amplitude, T_A (K)	25	25	12.5	25	25
Source T Period, τ (hours)	1	2	1	1	1
No. of Diodes, Masses	2, 2	2, 2	2, 2	1, 1	0, 0
Measured Average T_H $<T_H>$ (K)	343.7	342.1	334.4	345.7	325.0
Measured Average T_C $<T_C>$ (K)	305.5	305.9	314.1	325.1	325.0
Measured Abs. Avg. ΔT $<|T_H - T_C|>$ (K)	38.3	36.2	20.3	20.6	15.9
Percentage of Baseline $<|T_H - T_C|>$	100%	94.8%	53.1%	53.9%	41.6%
Measured Average Power $<P>$ (mW)	117.4	105.3	32.7	34.0	29.6*
Percentage of Baseline Power	100%	89.7%	27.9%	29.0%	25.2%*

These results clearly show the benefit of this rectification strategy. When compared to the baseline (Figure 6a), a "solar thermal" comparative case subject to the same temperature profile (Figure 6b) produces 29.0% the output power. At first glance, it would seem that holding the cold sink temperature at T_{avg} should produce 25% the output power of the fully rectified system, if the proposed $P \propto (\Delta T)^2$ rule applies. However, like the "amplitude dependence" test, the "solar thermal" assembly results in a periodically steady state ΔT (20.6 K) greater than 50% of the periodically steady ΔT of the "baseline" test (38.3 K), likely due to a higher constant T_C temperature. Squaring these temperature terms suggests a 28.9% power relation (compared to the observed 29.0%), again verifying the proposed $P \propto (\Delta T)^2$ model detailed fully in Figure 8(a). Finally, the completely non-rectified "waste heat scavenging" scheme (Figure 6c) results in the lowest power output of any configuration tested, even with the relatively higher power generation of its thermoelectric module, shown in Figure 8(b).
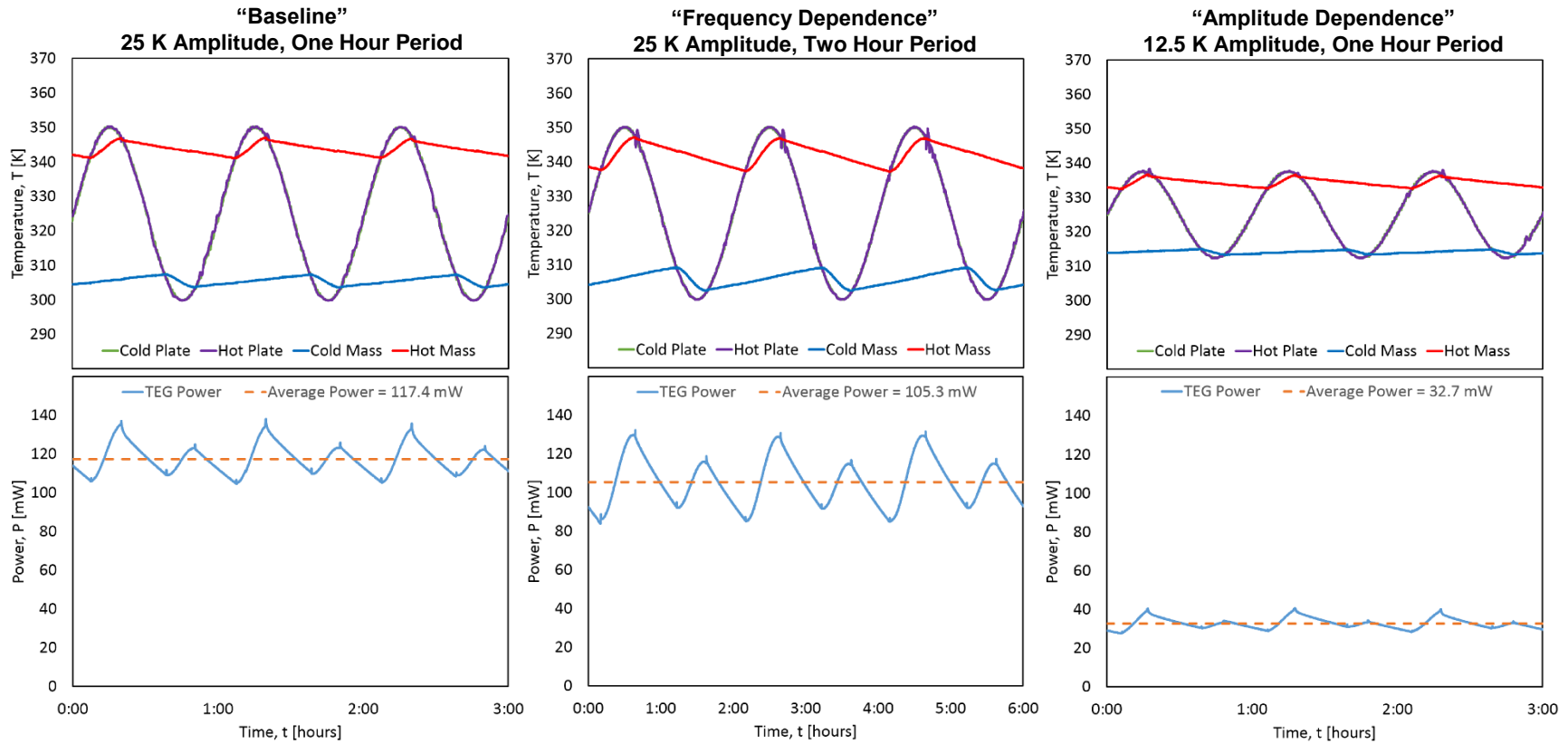
Figure 9. Comparison of the first three scenarios of Table 1. (left) "Baseline" testing source with 25 K amplitude and one hour period, corresponding to t = 4:00 to 7:00 in Figure 7. (center) "Frequency dependency" testing source with 25 K amplitude and two hour period. (right) "Amplitude dependency" testing source with 12.5 K amplitude and one hour period. In all cases, the upper plot shows plate and mass temperatures, and the lower plot displays resultant thermoelectric (TEG) power output. Longer thermal decay periods in the "frequency dependency" test result in 89.7% of "baseline" power output. Smaller temperature differential magnitudes in the "amplitude dependency" test result in 27.9% of "baseline" power output.
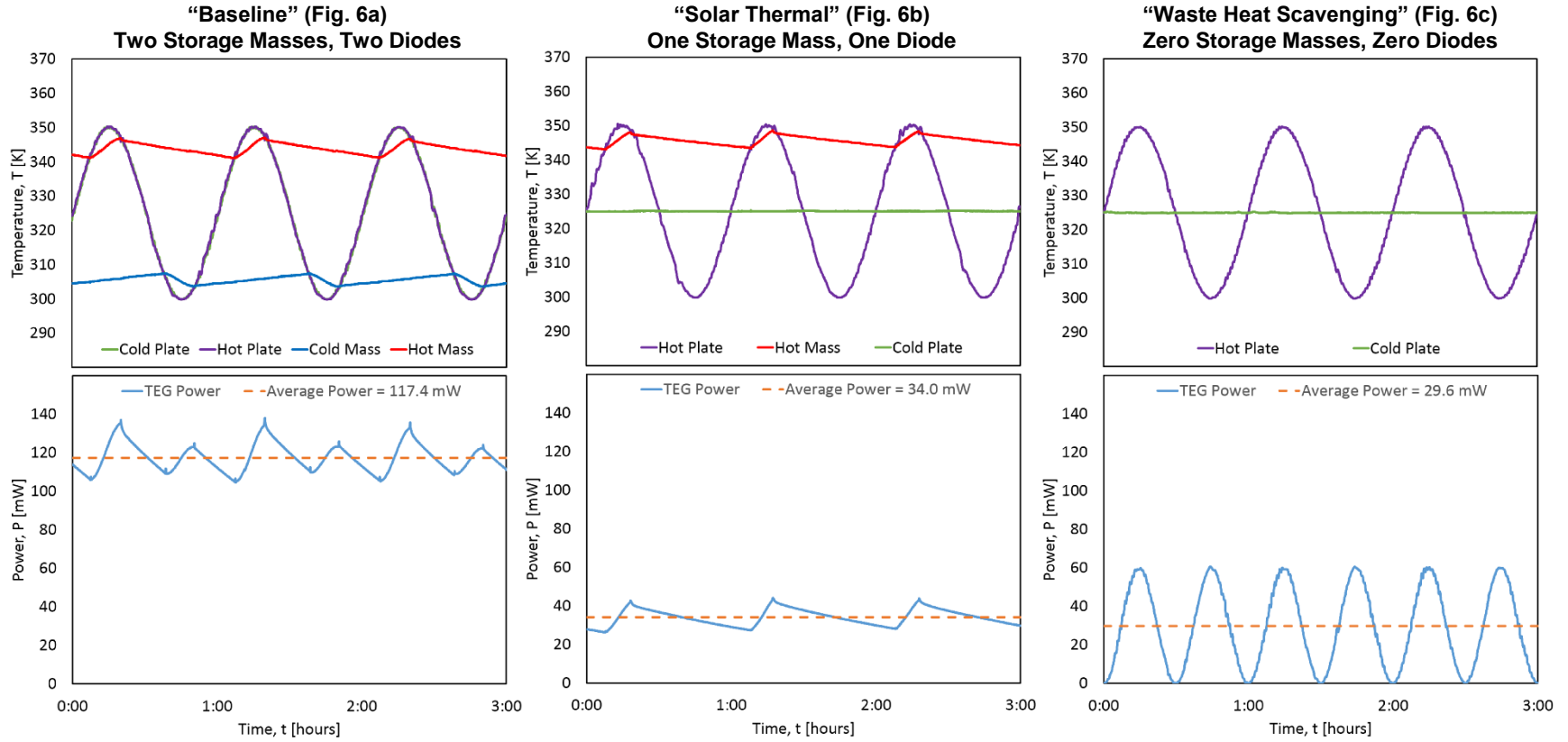
Figure 10. Comparison of the first, fourth, and fifth scenarios of Table 1. (left) "Baseline" testing scheme with two thermal storage masses and two thermal diodes, corresponding to t = 4:00 to 7:00 in Figure 7. (center) "Solar thermal" testing scheme with one thermal storage mass and one thermal diode. (right) "Waste heat scavenging testing scheme with zero thermal storage masses and zero thermal diodes. In all cases, the upper plot shows plate and mass temperatures, and the lower plot displays resultant thermoelectric (TEG) power output. Periodically steady power output of "solar thermal" and "waste heat scavenging" partially- or non-rectified cases are 29.0% and 25.2% that of a fully-rectified "baseline" scheme.

5 – Conclusion

A periodic thermal source was successfully rectified with the use of thermal diodes and mass storage in a novel thermal rectification assembly. The employment of "active" conduction-based thermal diodes enabled this concept, which was tested under a range of operating conditions and configurations. The magnitude of this rectification effect was examined with application-specific configurations, and the system sensitivity to changes in thermal signal frequency and amplitude was also demonstrated. Across all tests, thermal rectification was shown to enable more stable, continuous power generation from an oscillating temperature source. In addition, rectification allows for the utilization of maximum and minimum environmental temperatures, such as the hot solar noon and cold night sky, even if they are offset in time. This maximum temperature differential utilization increases heat engine power output according to the square of the temperature differential. This indicates even a small degree of rectification could have substantial impacts in power generation in solar thermal or other thermally-oscillating environments.

6 – Recommendations for Future Work

While testing this thermal rectification concept and assembly in a controlled laboratory setting allows for considerable manipulation of operating conditions such as temperature amplitude and frequency, this concept should be tested under real solar power generation conditions. Modification of this system for a "field" test should include an increase of the thermal mass storage capacity mc_p for the increased 24-hour period. An increase in insulation thickness should accompany the growth in thermal mass surface area, if increased environmental leakage is to be avoided. Analytical model results [1] indicate that a reduction of the forward diode thermal resistance can bring significant performance benefits, and an increased thermal mass size could be an opportunity to increase the diode contact area and reduce this resistance (keeping in mind the required contact pressure). Solar collector design is a non-trivial subject, and care should be taken to minimize any internal thermal resistances between the collector's surface and the thermal diode interface.

In addition, alternate diode and thermal storage mass concepts should be investigated. Most immediately, water appears to have a relatively high thermal storage density ρc_p. It's also relatively low-cost when compared with aluminum. Water does carry the risk of thermal gradients within its volume that aluminum, with its high thermal conductivity, does not. Additionally, liquid water can evaporate or leak, unlike a solid storage mass. However, this concept should still be explored further in future work.

7 – Acknowledgements

8 – References

1. Zhao, Xiaodong. *The Thermal Diode Bridge Applied on Solar Energy Harvesting.* MS Report, University of California at Berkeley. Berkeley, 2015.
2. Raman, Aaswath P., et al. "Passive radiative cooling below ambient air temperature under direct sunlight." *Nature* 515.7528 (2014): 540-544.
3. Rephaeli, Eden, Aaswath Raman, and Shanhui Fan. "Ultrabroadband photonic structures to achieve high-performance daytime radiative cooling." *Nano letters* 13.4 (2013): 1457-1461.
4. Zhu, Linxiao, et al. "Radiative cooling of solar cells." Optica 1.1 (2014): 32-38.
5. Catalanotti, S., et al. "The radiative cooling of selective surfaces." *Solar Energy* 17.2 (1975): 83-89.
6. Granqvist, C. G., and A. Hjortsberg. "Radiative cooling to low temperatures: General considerations and application to selectively emitting SiO films." *Journal of Applied Physics* 52.6 (1981): 4205-4220.
7. Roberts, Nick A., and D. G. Walker. "A review of thermal rectification observations and models in solid materials." *International Journal of Thermal Sciences* 50.5 (2011): 648-662.
8. Boreyko, Jonathan B., Yuejun Zhao, and Chuan-Hua Chen. "Planar jumping-drop thermal diodes." *Applied Physics Letters* 99.23 (2011): 234105.
9. Kobayashi, W., Y. Teraoka, and I. Terasaki. "An oxide thermal rectifier." *Applied Physics Letters* 95.17 (2009): 171905.
10. Chen, Zhen, et al. "A photon thermal diode." *Nature communications* 5 (2014).
11. Ben-Abdallah, Philippe, and Svend-Age Biehs. "Phase-change radiative thermal diode." *Applied Physics Letters* 103.19 (2013): 191907.
12. Miller, John, Wanyoung Jang, and Chris Dames. "Thermal rectification by ballistic phonons in asymmetric nanostructures." *ASME 2009 Heat Transfer Summer Conference collocated with the InterPACK09 and 3rd Energy Sustainability Conferences.* American Society of Mechanical Engineers, 2009.
13. MWH (2004). Green roof test plot: 2003 End of Year Project Summary Report. Prepared for the City of Chicago Department of Environment. Retrieved Dec. 01 2015 from http://www.cityofchicago.org/dam/city/depts/doe/general/GreenBldsRoofsHomes/2003GreenRoofReport.pdf